Photoacoustics 19 (2020) 100185

Contents lists available at ScienceDirect

Photoacoustics

journal homepage: www.elsevier.com/locate/pacs

Research article

Three-phase vaporization theory for laser-activated microcapsules

Guillaume Lajoinie[a,*], Mirjam Visscher[b,a], Emilie Blazejewski[c], Gert Veldhuis[c], Michel Versluis[a]

[a] Physics of Fluids Group, Technical Medical (TechMed) Center and MESA + Institute for Nanotechnology, University of Twente, P.O. Box 217, 7500 AE Enschede, The Netherlands
[b] Department of Biomedical Engineering, Thorax Center, Erasmus MC, PO Box 2040, 3000 CA Rotterdam, The Netherlands
[c] Nanomi Monosphere Technology, Zutphenstraat 51, 7575 EJ Oldenzaal, The Netherlands

ARTICLE INFO

Keywords:
Microcapsules
Thermodynamics
Vaporization
Cavitation
Bubble
Photoacoustics
Heat transfer

ABSTRACT

Precision control of vaporization, both in space and time, is critical for numerous applications, including medical imaging and therapy, catalysis and energy conversion, and it can be greatly improved through the use of micro- or nano-sized light absorbers. Ultimately, optimization of these applications also requires a fundamental understanding of the vaporization process. Upon laser irradiation, polymeric microcapsules containing a dye can vaporize, leading to the growth of a vapor bubble that emits a strong acoustic signature. Here, we compare laser-activated capsules containing either a volatile or a non-volatile oil core. We theoretically explore the vaporization of the capsules based on a three-phase thermodynamics model, that accounts for the partial vaporization of both the surrounding fluid and the oil core as well as for the interaction between heat transfer and microbubble growth. The model is compared to ultra-high-speed imaging experiments, where we record the cavitation events. Theory and experiments are in convincing agreement.

1. Introduction

Cavitation, defined as the formation, growth and collapse of bubbles in a liquid, is used in a multitude of applications including surface cleaning [1], mixing [2], as well as medical imaging and therapy. The formation of bubbles in a pure liquid requires extreme negative pressures to overcome the tensile strength of the liquid. For example, peak-negative pressures required to induce acoustic cavitation in distilled water [3] are typically 140 MPa, theoretically, and often over 30 MPa experimentally [4,5].

Cavitation nuclei and inhomogeneities, such as those typically found in human tissue, can lower the cavitation threshold towards less extreme peak negative pressures. A whole area in biomedical research focuses on facilitating nucleation through the use of microbubbles, nanoparticles or other cavitation nuclei for medical applications. These include kidney stone removal [6,7] through extracorporeal shockwave lihotripsy, accelerated clot lysis or sonothrombolysis [8], enhanced delivery and uptake of drugs, genes or viruses to cells and interstitial tissues [9–11], and embolotherapy by triggering the phase-change of liquid perfluorocarbon agents [12–14].

Despite the presence of facilitating agents, inducing cavitation by means of a pressure wave remains challenging. In contrast, localized heating provides an easier and more reproducible way to reach the vaporization threshold and is of interest for a similar range of applications. This observation triggered a deep interest for heat-induced, and in particular laser-induced, cavitation. A promising approach lies in the use of photoacoustic nanodroplets consisting of a perfluoropentane (PFP) core loaded with plasmonic nanoparticles and a stabilized by a serum albumin shell [15]. A pulsed laser then triggers a phase transition of the PFP, inducing vaporization. Plasmonic nanoparticles triggered by pulsed or CW laser excitation were proposed for cancer therapy [16,17], or as an alternative approach for light to steam energy conversion [18]. Alternative constructs consisting of light-absorbing microcapsules have also been designed to overcome the safety concerns associated to metallic nanoparticles, and proposed for therapy [19] and multimodal imaging [20]. While there is a clear interest for this type of light-absorbing particles and the resulting cavitation events, further development of innovative and effective systems would be greatly facilitated by a more detailed understanding of the physical phenomena at hand. In particular, the role of multiple liquid phases, e.g. oil and water, in the vaporization process, the strong coupling between heat transfer and ultrafast microbubble dynamics and the resulting acoustic activity require more investigation.

We have demonstrated before that light-absorbing microcapsules can vaporize the surrounding water upon laser irradiation [21] and have established the basic physical understanding for this type of systems by providing a simplified theoretical model. The system previously studied, however, is limited in its applicability by the combined high

* Corresponding author.
E-mail address: g.p.r.lajoinie@utwente.nl (G. Lajoinie).

https://doi.org/10.1016/j.pacs.2020.100185
Received 26 November 2019; Received in revised form 15 April 2020; Accepted 22 April 2020
Available online 23 May 2020

boiling point and large heat capacity of water.

A promising approach to further reduce the vaporization threshold consists in loading a low boiling point liquid in the capsule core, such as a perfluorocarbon [19,20]. Moreover, breaching the encapsulating shell also consumes energy, leaving less energy available for vaporization. A further lowering of the activation threshold could therefore be accomplished by partial encapsulation of a low boiling point liquid core, e.g. in a cup or acorn-shaped particle. The behavior of these multiphase systems cannot be described using our previous model [21].

Here, we want to investigate the physical mechanisms underlying the vaporization of three systems: (i) a capsule where the outer liquid preferentially vaporizes owing to a high boiling-point core, i.e. the system in Lajoinie et al. (2014), (ii) a capsule containing a low boiling-point core, that vaporizes preferentially over the surrounding water and (iii) a "cup" where the low boiling point core is only partially encapsulated in order to save the energy necessary to rupture the polymer shell. The mechanical response of these microparticles is investigated experimentally by means of ultra-high-speed imaging and their behavior is described theoretically using first a two-phase, then three-phase, thermodynamic model. The model is both more general and robust than that previously proposed [21]. More specifically, the present model encompasses the partial vaporization of both the oil core and the surrounding liquid in relation to the dynamics of the microbubbles in a weakly compressible medium. In addition, we greatly refine the treatment of heat transfer and define a thermal boundary layer that accounts for heat diffusion, vaporization/condensation at the interface, temperature changes in the gas and bubble dilation/compression. Experimental results and theory show good agreement, which opens interesting routes to describe a variety of more complex laser-activated vaporization systems.

2. Theory

2.1. Thermodynamics of the two-phase system

From a theoretical standpoint, the simplest microcapsule formulation consist of the high boiling point oil core variant [21], i.e. a capsule containing an oil whose vaporization temperature is much higher than that of water. In first approximation, the core is therefore assumed not to vaporize and the resulting bubble consists of pure water vapor. These capsules (hereafter referred to as "HighBP" for "High Boiling Point") can therefore be modeled using a 2-phase system. The vapor/liquid equilibrium is described by the Antoine law [22]:

$$P_g = 10^{A-\frac{B}{C+T_g}}, \tag{1}$$

where P_g is the gas pressure, T_g is the gas temperature and A, B and C are constants that are specific to the liquid considered [23], in this case water.

We follow the closed system, as depicted in Fig. 1a, between the times t and $t+\Delta t$ where a water layer of thickness dr vaporizes or condenses. Practically, dr is positive or negative during vaporization or condensation, respectively. The thermodynamics of this system can be derived using the change in enthalpy, described by the first thermodynamics principle, which writes:

$$\Delta h = Q(t+\Delta t) - Q(t) + W(t+\Delta t) - W(t), \tag{2}$$

where Q represents the heat gained by the system and W the work done by the pressure forces. Or, considering heating and phase change:

$$\begin{aligned}\Delta h &= h(t+\Delta t) - h(t)\\ &= (\mathrm{n}+\mathrm{dn})c_{p_w}\tilde{\mu}_w(T_g(\mathrm{t}+\Delta\mathrm{t}) - T_g(\mathrm{t})) + \mathrm{dn}\ h_{v_w}\tilde{\mu}_w,\end{aligned} \tag{3}$$

where n is the number of moles in the system, dn is the number of moles that vaporized during Δt ($dn \ll n$), c_{p_w} is the specific heat of water, $\tilde{\mu}_w$ is the molar mass of water, T_g is the temperature of the gas and h_{v_w} is the vaporization enthalpy. T_g is considered to be homogeneous in the layer for short Δt. Eqs. (2) and (3) then yield:

$$\frac{dh}{dt} = nc_{p_w}\tilde{\mu}_w\dot{T}_g + \dot{n}h_{v_w}\tilde{\mu}_w = \dot{Q} + \dot{W}, \tag{4}$$

with:

$$\dot{W} = -P_{R^+}\frac{\mathrm{dV}}{\mathrm{dt}} = -\left(P_g - \frac{2\sigma}{R} - \frac{4\mu\dot{R}}{R}\right)\dot{V}, \tag{5}$$

where σ is the surface tension and μ the dynamic viscosity of water, and R and $\dot{R}$ are the radius of the bubble and velocity of the vapor–liquid interface, respectively. V is the volume of the bubble, $\dot{V}$ is the volume change rate. P_{R^+} is the pressure just outside the bubble. Heat transfer can be written as:

$$\dot{Q} = \mathrm{P_i} - \mathrm{P}_\ell, \tag{6}$$

where P_ℓ is the loss of power through the vapor–liquid interface and $\mathrm{P_i}$ is the power provided to the bubble by the hot polymer. We assume that only the dye-doped polymer is able to absorb light, owing to the low optical absorption of the other components. The polymer subsequently provides thermal energy to support the growth of the vapor bubble. Because of the microscopic dimension of the capsules, we assume that the polymer is instantly and homogeneously heated by the laser pulse to a temperature T_{p0}. Although the absorption coefficient of the polymer is high, the extinction cannot exceed a few percent of the total laser energy at most at this scale, i.e. $\alpha e_p \ll 1$ with α the absorption coefficient and e_p the thickness of the polymer slab. Heat is then transferred into the vapor, increasing its pressure:

$$\mathrm{P_i} = S_p\lambda_p\frac{T_p - T_g}{\delta_p}. \tag{7}$$

Here, S_p is the surface area of the polymer, λ_p is the thermal conductivity of the polymer, T_p is the polymer temperature, and δ_p is the thermal boundary layer in the polymer.

The thermal boundary layer thickness in the polymer is simplified to:

$$\frac{1}{\delta_p(t)} = \frac{1}{\sqrt{D_p t}} + \frac{2}{e_p}, \tag{8}$$

with D_p the thermal diffusivity of the polymer. This expression, similar to that of a hot sphere, describes the fast diffusion dynamics at short times and the plateauing of the thermal boundary layer thickness at long times. In view of the complex fate of the polymer shell, which includes breaking and reshaping, using a more refined expression would only complicate the model with little added value.

In Eq. (6), P_ℓ represents the power lost at the vapor–liquid interface:

$$\mathrm{P}_\ell = \lambda_w 4\pi R^2(t)\frac{T_{g0} - T_a}{\delta(t)}, \tag{9}$$

with λ_w the thermal conductivity of water, R the radius of the gas bubble, T_{g0} the temperature of the gas at $\mathrm{t}=0$, T_a the ambient temperature far away from the bubble and $\delta(t)$ the thermal boundary layer thickness in the water surrounding the microbubble.

Combining Eqs. (4), (5), (6), (7) and (9) yields:

$$nc_{p_w}\tilde{\mu}_w\dot{T}_g + \dot{n}h_{v_w}\tilde{\mu}_w = P_\mathrm{i} - \mathrm{P}_\ell - \left(P_g - \frac{2\sigma}{R} - \frac{4\mu\dot{R}}{R}\right)\dot{V}. \tag{10}$$

Using the ideal gas law:

$$\dot{n} = n\left(\frac{\dot{P}_g}{P_g} + \frac{\dot{V}}{V} - \frac{\dot{T}_g}{T_g}\right), \tag{11}$$

Finally, substituting Eqs. (11) and (1) in Eq. (10) leads to a first differential equation governing the gas temperature:

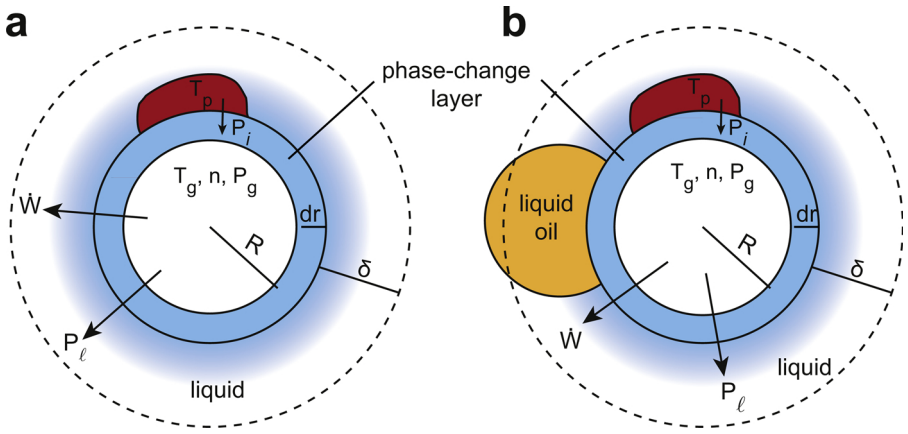

Fig. 1. Schematic representation of the thermodynamic model that describes the vaporization of microcapsules a. Microcapsule with a high boiling point core (two phase system) and **b**. microcapsule with a low boiling point core (three phase system).

$$\dot{T}_g = \frac{\left(\mathrm{P_i} - \mathrm{P}_\ell - \frac{h_{v_w} n \tilde{\mu}_w \dot{V}}{V} - \left(P_g - \frac{2\sigma}{R} - \frac{4\mu\dot{R}}{R}\right)\dot{V}\right)}{n\tilde{\mu}_w\left(c_{p_w} + \frac{h_{v_w}\,\mathrm{Bln}(10)}{(C+T_g)^2} - \frac{h_{v_w}}{T_g}\right)}, \tag{12}$$

where $\mathrm{P_i}$ is described by Eq. (7), P_ℓ is described by Eq. (9) and P_g is described by Eq. (1).

$\delta(t)$ is yet to be defined and collects all aspects of heat diffusion, change in the geometry of the system and condensation or vaporization. The thermal boundary layer thickness δ is influenced by 3 factors. First, a volume increase (or decrease) of the bubble in a spherical system redistributes the energy and thins (or thickens) the thermal boundary layer. Second, heat diffusion will add (or remove) thermal energy and finally, vaporization/condensation will directly affect the thermal boundary layer thickness. Writing the energy difference in the time interval *dt*:

$$\begin{aligned}\frac{E(t+\mathrm{d}t) - E(t)}{\mathrm{d}t} &= 2\pi R^2 c_{p_w}\rho_w \Delta T\left(\frac{\delta(t+\mathrm{d}t) - \delta(t)}{\mathrm{d}t}\right)\\ &\quad + 4\pi R\dot{R} c_{p_w}\rho_w \Delta T\delta(t).\end{aligned} \tag{13}$$

where E is the energy and ρ_w is the water density. This energy difference also corresponds to the heat diffusing out during the same time interval due to the temperature gradient at the bubble wall interface:

$$\frac{E(t+\mathrm{d}t) - E(t)}{\mathrm{d}t} = 4\pi R^2 \lambda_w \frac{\Delta T}{\delta}. \tag{14}$$

The change in boundary layer thickness due to condensation/vaporization can be derived from the vaporization rate:

$$\mathrm{d}V = 4\pi R^2 \mathrm{d}r = \frac{\dot{n}\tilde{\mu}_w}{\rho_w}, \tag{15}$$

with dV the volume of water undergoing phase change and *dr* the thickness of the vaporized liquid layer. Finally, combining Eqs. (13)–(15):

$$\dot{\delta} = \frac{2\lambda_w}{\rho_w c_{p_w}\delta} - \frac{2\dot{R}\delta}{R} - \frac{\dot{n}\tilde{\mu}_w}{4\pi\rho_w R^2}. \tag{16}$$

2.2. Thermodynamics of the three-phase system

When the oil core has a low boiling point, the system becomes a three phase system (liquid oil, liquid water and gas phase) and the bubble will consist of oil vapor and water vapor (Fig. 1b). These particles (hereafter referred to as “LowBP” for “Low Boiling Point”) must therefore be modeled using a 3-phase system in order to account for the effect of the core. The derivation for the three-phase system is identical, and we therefore provide only the modified equations.

The variation of enthalpy in the three-phase system writes:

$$\begin{aligned}\frac{\mathrm{dh}}{\mathrm{dt}} &= \dot{T}_g(n_c c_{p_c}\tilde{\mu}_c + n_w c_{p_w}\tilde{\mu}_w) + \dot{n}_c h_{v_c}\tilde{\mu}_c + \dot{n}_w h_{v_w}\tilde{\mu}_w\\ &= \mathrm{P_i} - \mathrm{P}_\ell - \left(P_g - \frac{2\sigma}{R} - \frac{4\mu\dot{R}}{R}\right)\dot{V},\end{aligned} \tag{17}$$

where n_c is the number of moles of oil vapor, n_w the number of moles of water vapor, c_{p_c} the specific heat of the core oil, c_{p_w} the specific heat of the water, $\tilde{\mu}_c$, the molar mass of the oil, $\tilde{\mu}_w$, the molar mass of the water, h_{v_c} the vaporization enthalpy of oil and h_{v_w} the vaporization enthalpy of water.

Rewriting Eq. (17) yields the following differential equation for T_g:

$$\dot{T}_g = \frac{\mathrm{P_i} - \mathrm{P}_\ell - \left(P_g - \frac{2\sigma}{R} - \frac{4\mu\dot{R}}{R}\right)\dot{V} - \dot{n}_c h_{v_c}\tilde{\mu}_c - \dot{n}_w h_{v_w}\tilde{\mu}_w}{n_c c_{p_c}\tilde{\mu}_c + n_w c_{p_w}\tilde{\mu}_w},$$

where $\mathrm{P_i}$ and P_ℓ are defined as in Eq. (7) and Eq. (9). P_g is the gas pressure, that we describe using the definition of the partial pressures:

$$P_g = \frac{n_c}{n}P_c + \frac{n_w}{n}P_w, \tag{18}$$

where P_c is the partial pressure of the core material (i.e. the oil) and P_w is the partial pressure of water. Using the perfect gas law, the thermal boundary layer for the three phase system becomes:

$$\dot{\delta} = \frac{2\lambda_w}{\rho_w c_{p_w}\delta} - \frac{2\dot{R}\delta}{R} - \frac{\dot{n}_w\tilde{\mu}_w}{4\pi\rho_w R^2} - \frac{\dot{n}_c\tilde{\mu}_c}{4\pi\rho_c R^2}. \tag{19}$$

Moderate laser energies will lead to a partial vaporization of the oil that then remains in equilibrium with its vapor. $\dot{n}$ in Eq. (16) now consists of two contributions for the water and the oil, represented by $\dot{n}_w$ and $\dot{n}_c$, respectively. Using Antoine's equation to calculate P_c and P_w and their time derivatives, differentiating the ideal gas law and combining leads to the differential equation:

$$\dot{n}_i = n_i\left(\frac{\dot{V}}{V} + \dot{T}_g\left(\frac{B_i\ln(10)}{(T_g + C_i)^2} - \frac{1}{T_g}\right)\right), \tag{20}$$

where $i = w$ or c, stands for the water or the core material (i.e. the oil). Finally:

$$\dot{P}_g = \frac{\dot{T}_g}{n}\left(\frac{B_c n_c \ln(10)}{(T_g + C_c)^2}(2P_c - P_g) + \frac{B_w n_w \ln(10)}{(T_g + C_w)^2}(2P_w - P_g) + \frac{n_c(P_g - P_c) + n_w(P_g - P_w)}{T_g}\right) + \frac{\dot{V}}{nV}(n_c(P_c - P_g) + n_w(P_w - P_g)). \quad (21)$$

Note that in practice, the oil is contained in the core of the capsule and is therefore available only in limited amount.

In case of complete vaporization, the ideal gas law is used to calculate the partial pressure of the oil vapor, reducing Eq. (21) to:

$$\dot{P}_g = \frac{\dot{T}_g}{n}\left(\frac{\ln(10) B_w n_w}{(T_g + C_w)^2}(2P_w - P_g) + \frac{n_c P_c + n_w(P_g - P_w)}{T_g}\right) + \frac{\dot{V}}{nV}(n_c P_c + n_w(P_w - P_g)). \quad (22)$$

2.3. Momentum

The backbone of the derivation is momentum conservation in spherical coordinates, i.e. a Rayleigh-Plesset-type equation that connects the gas pressure in the bubble to dynamics of the bubble radius. Here, we use the Keller-Miksis equation [24], also derived by Prosperetti and Lezzi [25]:

$$\left(1 - \frac{\dot{R}}{c_l}\right)R\ddot{R} + \frac{3}{2}\left(1 - \frac{\dot{R}}{3c_l}\right)\dot{R}^2 = \frac{1}{\rho}\left[\left(1 + \frac{\dot{R}}{c_l}\right)\left(P_g - P_{\text{atm}} - \left(\frac{2\sigma}{R} + \frac{4\mu\dot{R}}{R}\right)\right) + \left(\frac{R}{c_l}\dot{P}_g\right)\right]. \quad (23)$$

with c_l the speed of sound in the liquid. Note that we neglect the small effect of the interfacial terms on the acoustic radiation term $\frac{R}{\rho c_l}\dot{P}_g$. In our derivation, the polymer is assumed not to influence the dynamics of the vapor/liquid interface.

Eqs. (12), (19), (21) and (23) (alternatively Eqs. (12), (16), (1) and (23) now form the set of coupled differential equations that can be integrated to obtain the radius-time curve of the cavitation bubble, with the associated temperature and pressure fields.

3. Materials and methods

3.1. Materials

Sodium cholate hydrated, Polyvinyl alcohol (PVA), Poly(lactide-co-glycolide) Resomer RG502 (MW 7–17 and MW 28–34), Poly(methyl methacrylate) (MW 120,000), Hexadecane, Sudan Red, Nile Red and Dichloromethane (ACS reagent) were purchased from Sigma-Aldrich (St. Louis, MO, USA). PDLG 5002, PDLG 5004 and PDL 02 were supplied by Purac. Perfluoropentane (PFP) was purchased from Fluorochem (UK). Tween 20 was purchased from VWR (The Netherlands).

3.2. Capsules production method

Hexadecane-loaded PMMA microcapsules were prepared by a emulsion solvent evaporation technique, using microsieve emulsification [26]. Prior to emulsification, hexadecane (boiling point, T_b = 286 °C), PMMA (glass transition temperature, T_{glass} = 103 °C) and dye were dissolved in dichloromethane. The final oil concentration was 2.16% w/w. The dye concentration was either 3 or 5% w/w.

Resomer microcapsules containing perfluoropentane were fabricated in a similar way as the PMMA capsules. Resomer (T_{glass} = 50 °C) was dissolved into dichloromethane along with perfluoropentane (T_b = 29 °C) and dye and placed in a 20 °C bath to ensure the full miscibility of the oil in dichloromethane. Ultrapure water containing an emulsifier (PVA 4% (w/w) or SC 1.5% (w/w)) maintained below 15 °C was used as continuous phase. The final oil concentration was 2.42% w/w and dye concentration was 5% w/w.

The solutions were filtered through a 0.45 µm PTFE filter and emulsified through a microsieve membrane (Nanomi B.V., The Netherlands) with uniform pores along the surface. The emulsions were then spread into an aqueous solution containing an emulsifier. This was left to stir at room temperature for at least 3 h to evaporate the dichloromethane. The hardened microcapsules were concentrated and washed repeatedly by using a vacuum filtration and using an 0.05% w/w Tween 20 solution. Subsequently, the washed suspension was stored at 4 °C.

For the remainder of this paper, we will refer to the high boiling-point PMMA-Hexadecane capsules as highBP capsules and to the low boiling-point resomer-PFP capsules as lowBP capsules.

Acorn shaped particles were also produced with the same formulation as the Resomer-PFP capsules except for a slightly higher molecular weight of the Resomer, and will be referred to as lowBP cups in this paper. The cups are used to study the importance of particle geometry.

3.3. Particle characterization

Scanning Electron Microscopy (SEM) was performed using a JEOL JCM-5000 (NeoScope) operating between 5 and 15 kV in high vacuum mode. Particles were coated with NeoCoater MP-19020 NCTR. Before imaging, particles were washed by filtration in order to remove the excess of surfactant which can interfere and decrease the quality of the SEM recordings.

A Beckman Coulter Counter (Multisizer 3) was used to determine the particle size distribution (PSD). Data was recorded and statistically treated by Multisizer™ 3.53 software. ISOTON® diluent was used as electrolyte, and a aperture tube of 50 µm was used.

3.4. Numerical modeling

Integration of the set of differential equations was performed in Matlab® using the stiff ODE solver 15 s. The set of physical properties used in the simulation is provided in Table 1. We compute the model for initial polymer temperatures (T_{p0}) ranging from 308 to 673 K by increments of 5 K, where the highest temperature corresponds to the critical temperature of water. During numerical simulation, the surface tension was set to zero when the cavitation nucleus is smaller than the capsule to represent the shielding of the bubble nucleus by the polymer shell.

The influence of three parameters was investigated. First, the inital temperature of the surrounding liquid (T_a). Second, the ratio of the inner to outer radii of the capsules is varied from 0.1 to 0.9. Finally, the external radius was varied, from 500 nm up to 10 µm. The default values and the range used in the simulation for each parameter is given in Table 2.

3.5. Setup and experimental methods

A suspension of microcapsules was injected into an Opticell and a single microcapsule was located through a water-immersion objective (60×, NA = 0.9 Olympus). The capsules were excited with an 8 ns laser pulse at a wavelength of 532 nm (Quantel Evergreen 150 mJ). HighBP capsules were irradiated only once, since no further response was expected at multiple excitations. LowBP capsules and cups are both irradiated three times. Optical imaging was performed using the

Table 1
List of material properties: list and values of the material properties appearing in the model, and necessary for the simulation of the cavitation dynamics.

Parameter	Symbol	Value	Unit
Antoine coefficient A (water)		3.55959	/
Antoine coefficient B (water)		643.748	/
Antoine coefficient C (water)		−198.043	K
Antoine coefficient A (PFP)		4.38423	/
Antoine coefficient B (PFP)		1257.758	/
Antoine coefficient C (PFP)		−13.231	K
Vaporization enthalpy (water)	h_{v_w}	function of temp. (webbook, NIST)	$J.kg^{-1}$
Vaporization enthalpy (PFP)	h_{v_c}	93,950	$J.kg^{-1}$
Molar mass (water)	$\tilde{\mu}_w$	18.10^{-3}	$kg.mol^{-1}$
Molar mass (PFP)	$\tilde{\mu}_c$	0.288	$kg.mol^{-1}$
Specific heat (water)	c_{p_w}	4186	$J.K^{-1}.kg^{-1}$
Specific heat (PFP)	c_{p_c}	653.8	$J.K^{-1}.kg^{-1}$
Surface tension water	σ	function of temp. (webbook, NIST)	$N.m^{-1}$
Dynamic viscosity (water)	μ	10^{-3}	Pa.s
Thermal conductivity (polymer)	λ_p	0.17	$W.m^{-1}.K^{-1}$
Thermal conductivity (water)	λ_w	0.61	$W.m^{-1}.K^{-1}$
Heat diffusion area (polymer)	S_p	$4/\pi R_i^2$	m^2
Shell thickness	e_p	$R_e - R_i$	m
Diffusivity (polymer)	D_p	$1.36.10^{-7}$	$m^2.s^{-1}$
Ambient temperature	T_a	293	K
Density (water)	ρ_w	10^3	$kg.m^{-3}$
Density (PFP)	ρ_c	1630	$kg.m^{-3}$
Atmospheric pressure	P_{atm}	10^5	Pa

Table 2
Default value and parameter range for the numerical simulation. T_a is the temperature of the surrounding liquid, R_{ext} is the external radius of the microcapsules, and R_{int} is its internal radius.

	Default value	Parameter range
T_a	293 K	273–323 K
R_{ext}	3 μm	500 nm–10 μm
$\frac{R_{int}}{R_{ext}}$	0.8	0.1–0.9

Brandaris 128 ultra-high-speed camera [27,28] operated at a speed of 10 million fps (128 images per recording; FOV 34 × 47 μm), the sample was illuminated using a Xenon strobe light. The acoustic emissions in response to laser activation were recorded with a focused broadband 1 MHz US transducer (C302 Panametrics), see Fig. 2. The US signals were amplified using a pulser/receiver (Olympus model 5077PR). Single capsules were located using a CCD camera (Lumenera LM165M) and light source (KLed 2500, Schott), coupled through the Xenon strobe light. The experiment was performed at various laser energies to find the threshold for vaporization and quantify the statistical behavior of the microcapsules. Experiments were performed at 20 °C.

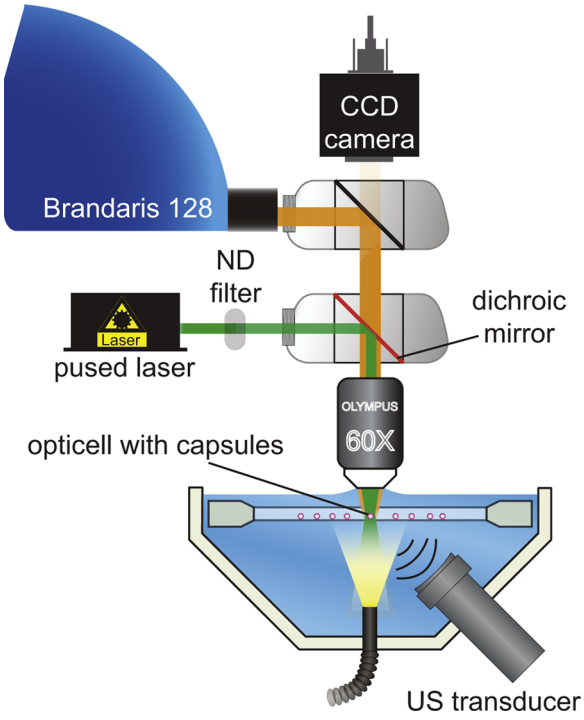

Fig. 2. Setup Schematic. Schematic of the ultra-high speed imaging setup, combining optical and acoustical detection. The laser beam is focused through the microscope onto a single microcapsule contained in an Opticell. The response is recorded using the Brandaris 128 camera at a speed of 10 to 15 million frames per second. The acoustical response is recorded by a broadband focused 1 MHz transducer.

The optical data was analyzed using Matlab®. The area A covered by the capsule and the produced bubble within the recorded frames was determined through thresholding and, assuming spherical bubbles, was used to determine the equivalent bubble radius through $R = \sqrt{\frac{A}{\pi}}$. When analyzing the radius-time curves, 2 situations can arise. In case (1), either the capsule is separated from the bubble (Fig. 6, II and III) or the bubble fully overlaps with the polymer shell (Fig. 7). In this case, the polymer does not interfere with the bubble size detection. In case (2), the polymer is intact and attached to the bubble (Fig. 8), in which case the detected area corresponds to the area covered by the polymer plus that covered by the bubble. Each individual case has been categorized into cases (1) or (2). The correction for case (2) consists in using the first reference recording (no laser excitation) from which we determine the area covered by the polymer. This area is then subtracted from what is detected in the subsequent recordings with the laser ON.

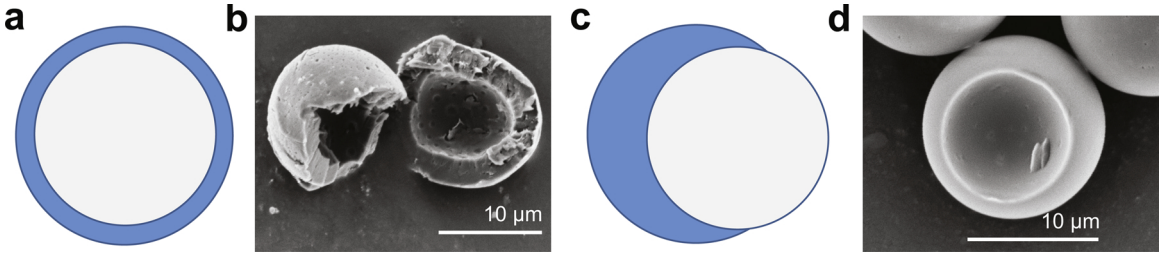

Fig. 3. Different microcapsule morphologies that can result from emulsion based phase separation.(a) Schematics of a capsule that contain a low (perfluoropentane) or high (hexadecane) boiling point and **(b)** SEM image of such a capsule. **(c)** Schematic and **(d)** SEM image of a cup.

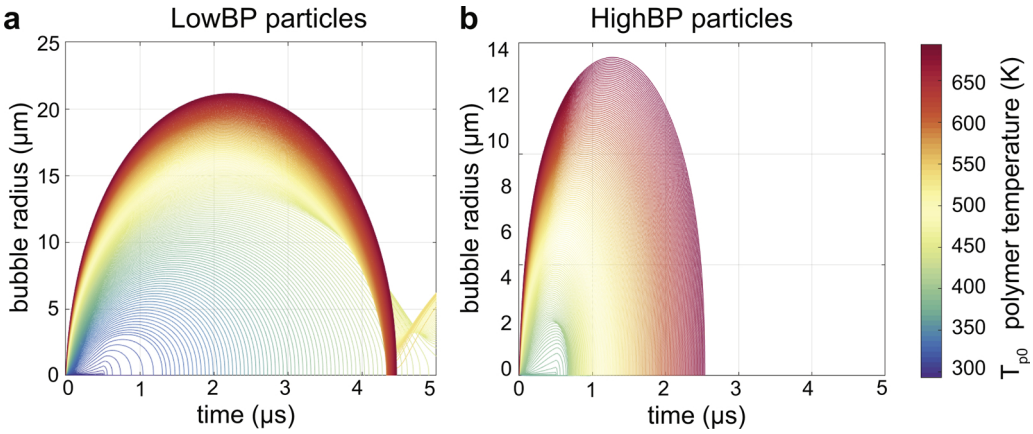

Fig. 4. Radius-time curves. Radius-time curves computed for (**a**) lowBP capsules (Resomer-PFP) and (**b**) highBP capsules (PMMA-hexadecane. The particles size is the nominal size of the capsules produced for the study.

4. Results

4.1. Vaporization dynamics (numerics)

The highBP capsule has a PMMA, polymer shell with a thickness of approximately 600 nm, a hexadecane core and a radius of 3 μm (PDI 10%), very similar to our earlier work [21], resulting in a ratio $\frac{R_{int}}{R_{ext}}$ of 0.8. The lowBP capsules have a radius of 2.5 μm (PDI 10%), and were formulated so as to have comparable proportions, i.e. $\frac{R_{int}}{R_{ext}} = 0.8$, see SI1. SEM images of the capules and cups are shown in Fig. 3.

The model, as derived above, requires 3 parameters in order to predict the behavior of the capsules: ambient temperature, radius of the capsules and amount of polymer (i.e. the ratio of inner to outer radius of the shell). The effect of laser heating is described in terms of initial temperature of the polymer shell. Since the lowBP capsule formulation and the cups contain the same amount of polymer and oil, they are numerically indistinguishable (note that the model focuses on the vaporization dynamics after nucleation). Fig. 4 provides a visualization of the model for both types of particles with standard sizes and shell thicknesses, see SI1 for the size distribution of the capsules. The response of the bubbles is provided as a function of time and initial polymer temperature. The lowBP capsule generates larger bubbles (20 μm versus 14 μm for the highBP capsule) and the threshold for activation lies at lower temperatures: 380 K for the highBP capsules versus 320 K for the lowBP capsules.

In a first set of simulations, we investigate the effect of ambient temperature, which was varied from 273 K to 323 K in increments of 5 K. The external radius, R_{ext} is kept constant at 3 μm and the ratio of the inner to outer shell radius is set to 0.8. The impact on the cavitation dynamics is shown in Fig. 5a and b. Increasing the ambient temperature T_a in the model has two effects. First, it reduces the difference between the initial temperature of the liquids and their boiling temperatures and thus increases the fraction of energy that can be used for vaporization with respect to heating. Second, increasing the ambient temperature decreases the temperature difference between the bubble produced and the surrounding liquid, thereby reducing heat loss from the bubble towards the water bath. The lowBP capsules (Fig. 5a) display a steep response when the temperature of the water bath comes close to the boiling point of the oil ($T_b \sim 302$ K). For the highest temperature, the microcapsules' response display a quasi plateau. For the high boiling

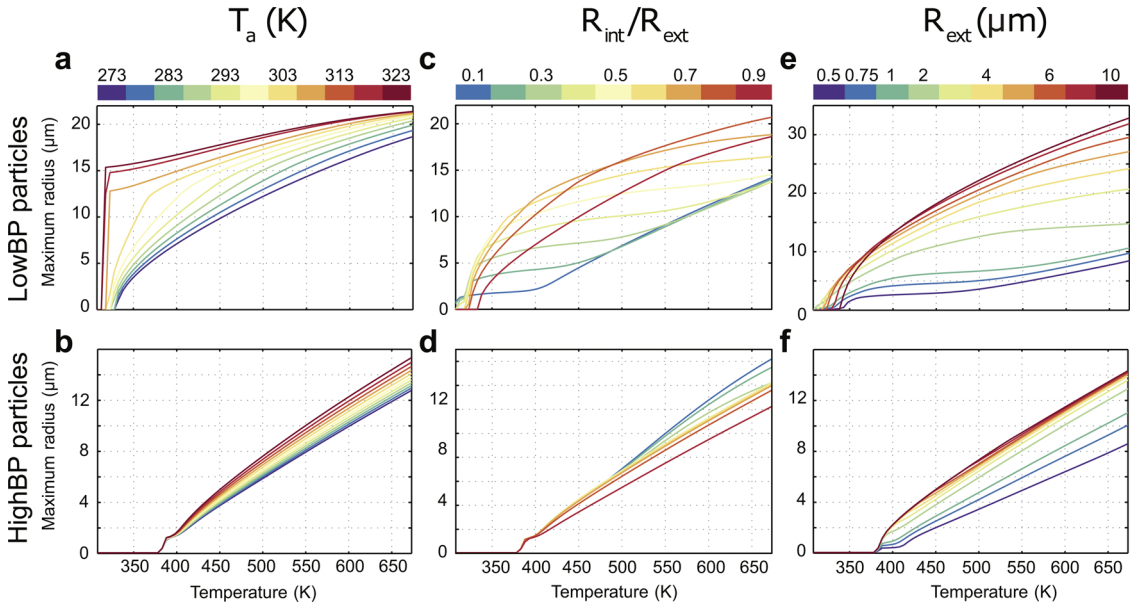

Fig. 5. Parameter study based the theoretical model. Maximum predicted radius for different liquid temperatures (T_a) for (**a**) lowBP (Resomer-PFP) and (**b**) highBP (PMMA-Hexadecane) capsules, $R_{ext} = 3$ μm and $R_{int}/R_{ext} = 0.8$. Maximum predicted radius for different inner and outer radii ratios (R_{int}/R_{ext}) for (**c**) lowBP capsules and (**d**) highBP capsules, $T_a = 293$ K and $R_{ext} = 3$ μm. Maximum predicted radius for different external radii (R_{ext}) for (**e**) lowBP and (**f**) highBP, $T_a = 293$ K and $R_{int}/R_{ext} = 0.8$.

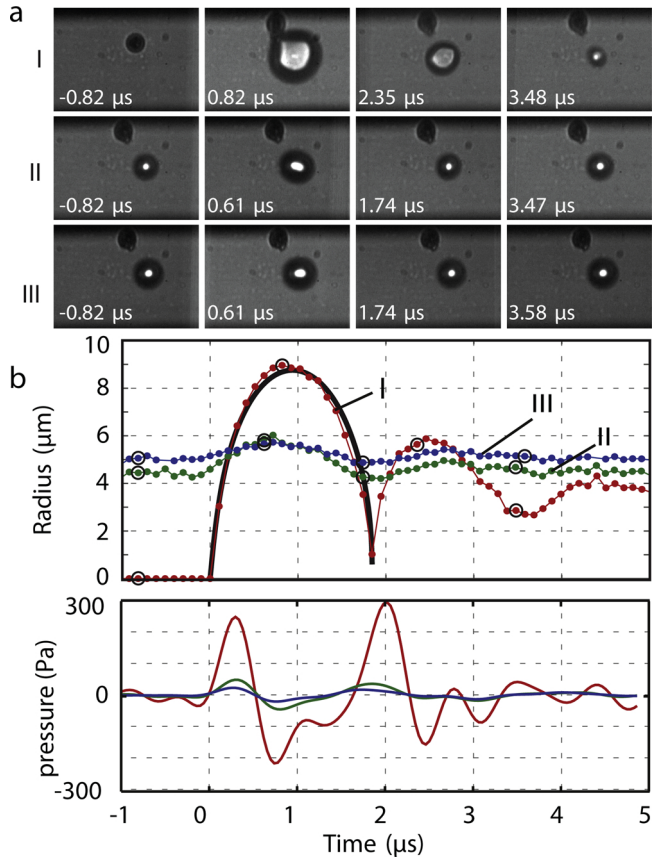

Fig. 6. Radius-time curves and waveforms lowBP capsules (Resomer-PFP) **(a)**Example responses of lowBP capsules where the bubble detaches from the capsule, but remains transiently stable and show little response in the following laser irradiations. The numbers I to III correspond to the laser irradiation number. **(b)**The corresponding radius-times curves and acoustic traces are plotted in the lower panel. The solid black line is the best fit to the model for the first laser exposure as a function of the initial polymer temperature obtained for T_p = 404 K and a PFP content fraction of 48%.

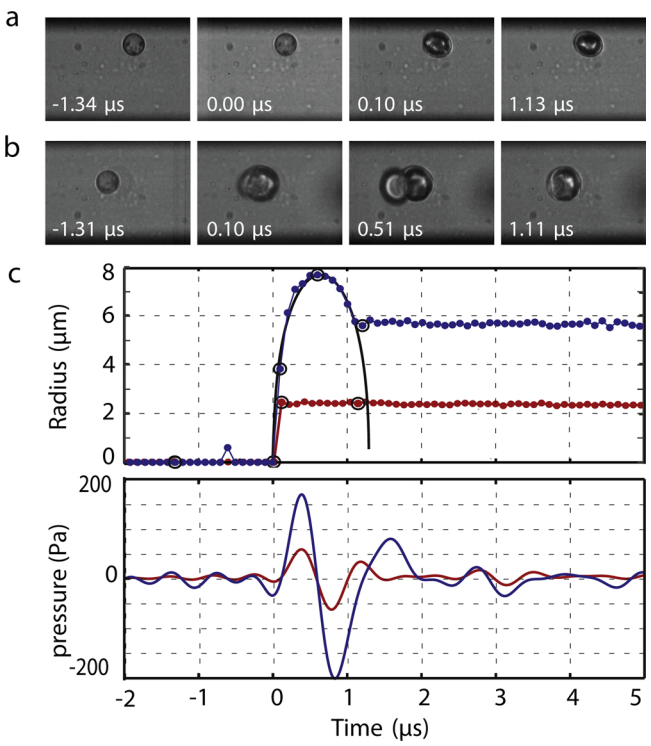

Fig. 7. Radius-time curves and waveforms highBP (PMMA-Hexadecane) capsules. Example responses of two distinct highBP capsules where (**a**) the capsule forms an internal bubble and (**b**), the capsule forms an external bubble. (**c**) Corresponding radius-times curves and acoustic traces are plotted in the lower panel. The solid black line is the best fit to the model for the first laser exposure as a function of the initial polymer temperature obtained for T_p = 644 K. Each of the particle type is loaded with 5% w/w dye.

point capsules (Fig. 5b), the bubble size increases by about 10% when increasing the ambient temperature to 323 K. Since the vaporization enthalpy of the water is high, this increase is mostly a consequence of the reduction of energy loss by heat diffusion.

The second set of numerical simulations investigates the effect of changing the inner to outer radius ratio, i.e. the ratio of polymer and oil contained in the capsule. The ambient temperature is kept constant at 293 K and R_{ext} is kept constant at 3 µm. The volume of polymer influences the amount of heat absorbed and therefore, the amount of energy available for vaporization, see Eq. (7). The lowBP capsules (Fig. 5c), display a very specific trend when changing the ratio R_{int}/R_{ext}. The maximum bubble radius increases rapidly, then reaches a plateau before displaying a second fast increase in the size of the cavitation bubble as a function of the initial polymer temperature. LowBP oil capsules benefit from an optimal balance between the amount of oil and polymer to reach the highest response, which occurs for a ratio of 0.7–0.8. In contrast, changing the ratio R_{int}/R_{ext} has little influence on the vaporization of highBP capsules (Fig. 5d): an increase of the ratio R_{int}/R_{ext} from 0.1 to 0.9 only reduces the diameter of the cavitation bubble by 25%. This counter-intuitive behavior results from the combination of high energy required to vaporize water with a slower thermal exchange between the thick shell and the bubble.

The third and last set of numerical simulations investigates the effect of particle size, which influences both the amount of deposited energy and of oil available for vaporization. To a lower extent, increasing R_{ext} also increases the surface area of the polymer, and thus its capacity to exchange heat with the bubble. The latter is a quadratic effect whereas the amount of oil has a cubic effect. The ambient temperature is kept constant at 293 K and the ratio of inner to outer shell radius was set to 0.8. The results are shown in Fig. 5e and f. As expected, the response of both highBP and lowBP capsules increases with increasing radius. In the case of highBP capsules, the response mostly saturates for capsules above 3 µm radius (Fig. 5f). The gain in the response of lowBP capsules becomes marginal when increasing the capsule radius above 4 µm. Note that the capsules fabricated for this study are 3 µm and 2.5 µm for highBP and lowBP capsules, respectively.

4.2. Experimental vaporization dynamics

Typical radius-time curves and corresponding acoustic emission waveforms recorded in ultra-fast imaging experiments are shown in Figs. 6–8 for the lowBP capsules, highBP capsules and cups, respectively. In each case, the best fit to the model is shown by the solid black line, and is in good agreement with the observations.

Fig. 6 displays a recording where a transiently stable bubble remains after a first exposure to a 120 mJ/cm^2 laser pulse but reacts mildly in the second and third exposures, most likely because the bubble containing the oil vapor detaches from the polymer, thereby preventing an efficient heating of the oil and its vapor.

HighBP capsules can produce two different types of bubbles, an “internal” and an “external” bubble. Fig. 7a provides an example of an internal bubble, i.e. a bubble produced without breaking the polymer shell, produced at a 1200 mJ/cm^2 laser pulse. Note the dramatically higher energy requirement. Application-wise, creating a bubble inside the shell is of limited interest and is therefore not investigated in depth here. An example of another capsule, producing an external bubble is displayed in Fig. 7b, produced at a 3800 mJ/cm^2 laser pulse. Unlike the

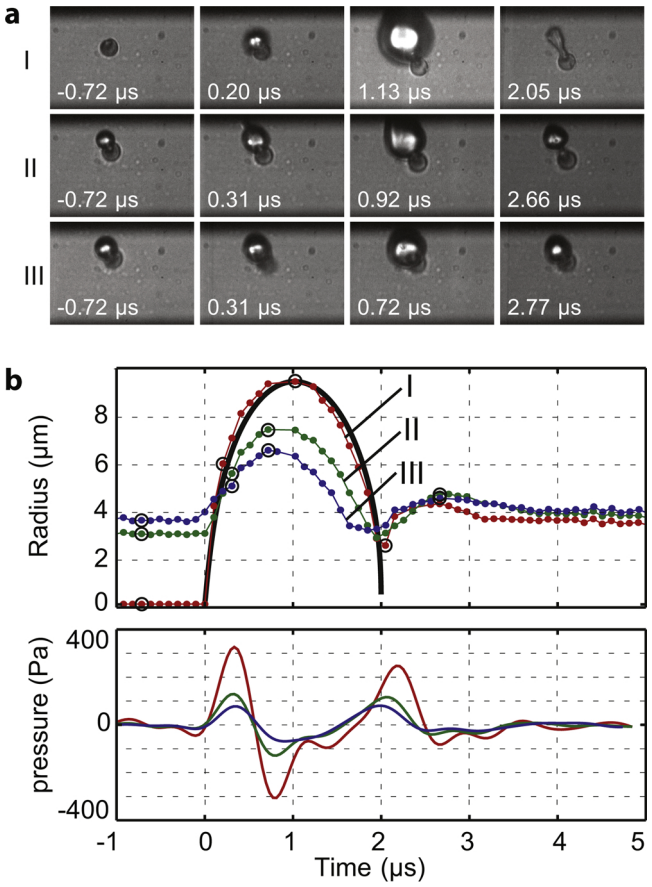

Fig. 8. Radius-time curves and waveforms lowBP (Resomer-PFP) cups. (**a**) Example responses of lowBP cups where the cup forms a stable bubble that remains attached to the polymer and displays a decreasing response when repeating the laser irradiation. The numbers I to III correspond to the laser irradiation number. (**b**) The corresponding radius-times curves and acoustic traces are plotted in the lower panel. The solid black line is the best fit to the model for the first laser exposure as a function of the initial polymer temperature obtained for T_p = 458 K and a PFP content fraction of 48%.

lowBP capsules, the highBP capsules hardly produce any bubbles that survive the initial inertial collapse.

For Resomer-PFP cups, the polymer shell does not fully encapsulate the oil. As a consequence, the polymer shell does not have to break in order to release the oil core and form a bubble. Typical radius-time curves for cups, shown in Fig. 8, produced at a 240 mJ/cm^2 laser pulse. Fig. 8 shows a bubble that survives the initial inertial collapse and remains attached to the shell, still active in exposures II and III. On rare occasions, the bubble response can increase with the number of exposures.

4.3. Statistical behavior

The response of each type of microparticles (loaded with 5% dye) at each laser energy was recorded multiple times in order to quantify the variability. This resulted in the distributions shown in Fig. 9. Fig. 9b confirms that the intensities required for the activation of a highBP capsule is much higher than for a lowBP capsule or cup (Fig. 9a and c). The threshold for bubble formation for highBP capsules lies around 1200 mJ/cm^2.

LowBP particles produce significantly larger bubbles, as large as 17 µm in radius, which is in good agreement with theory. The activation threshold of these capsules is 38 mJ/cm^2, see Fig. 9a. At high energy levels, the expansion of the bubble is so violent that the polymer shell is torn apart and possibly degraded, resulting in a greatly reduced response in the second and third exposures. The threshold for bubble formation for lowBP cups was not determined experimentally but lies below 60 mJ/cm^2, the lowest fluence used experimentally.

LowBP microcapsules were irradiated three times to monitor the evolution of their response. The resulting statistics are shown in Fig. 10 for a fluence of 120 mJ/cm^2. During the second and third exposures, the bubble produced becomes gradually smaller, which is attributed to the destruction of the agent.

4.4. Comparison of the numerical model to experimental data

Fig. 11 shows the lifetime of the bubble as a function of the maximum bubble radius for both numerical and experimental data. The lifetime is extracted from the radius-time curves and defined as the duration of existence of the cavitation bubble, not including possible after-bounces.

It is clear from the model, represented in Fig. 4, that (i) the initial polymer temperature is the only relevant parameter to compute the dynamics of the microbubble and (ii), that any initial polymer temperature leads to a unique radius-time curve. This initial temperature is proportional to the product of the optical absorption of the polymer and the laser energy. For a given capsule size and ambient temperature, there is therefore a unique relation between the maximum bubble radius and its lifetime. This relation does not depend on the laser energy or dye concentration but can be sampled by changing either one of these parameters. Given the small impact of the particle morphology (owing to the short timescale of heat diffusion from the polymer to the bubble), the cups will follow the same relation between the bubble lifetime and the maximum bubble radius as the capsules.

In the case of lowBP particles, the theoretical model predicts a significantly longer lifetime for large bubbles than observed experimentally, see Fig. 11a. The numerical integration was repeated with a reduced amount of oil in the core, namely 10%, 40%, 60% and 100% of the volume expected from the capsules formulation. The experimental data are spread between the theoretical lines obtained for oil core volumes of 10% to 60%. The theory for highBP capsules (Fig. 11b) shows a good agreement with the experimental results. The grey area represents the variation in the model predictions when accounting for the size distribution of the particles, as measured with the coulter counter (see SI1). In Fig. 11b, a collection of data points presents a significant maximum bubble radius but no lifetime. These are the internal bubbles (see Fig. 7a), where a stable bubble appears within the polymer shell.

The center-frequency of the emitted acoustic signals is plotted against the bubble lifetime in Fig. 12. This complementary aspect is representative of the acoustic capabilities of the particles, which is essential for many applications, and in particular medical applications since the acoustic emissions allow for locating and imaging the microcapsules. Furthermore, the acoustic signature is the only parameter that is remotely accessible to quantify the activation of the microcapsules. From Fig. 12a, it is obvious that a subpopulation of the PFP-filled particles does not follow the expected trend. This population includes the smallest and shortest-lived bubbles that, instead, follow the water-vaporization curve (i.e. the dashed line). This finding in consistent with bubbles that would be unable to access the expected volume of PFP, leading to the production of smaller bubbles that display the same dynamics as water vapor bubbles. A small quantity of PFP would only reduce the nucleation threshold and subsequently prevent the water from superheating. The precise mechanisms at play here require further investigation. The model is otherwise able to adequately describe the non-trivial vaporization dynamics of the laser-activated particles and provides a possibility for remote non-optical sizing of the cavitation bubbles.

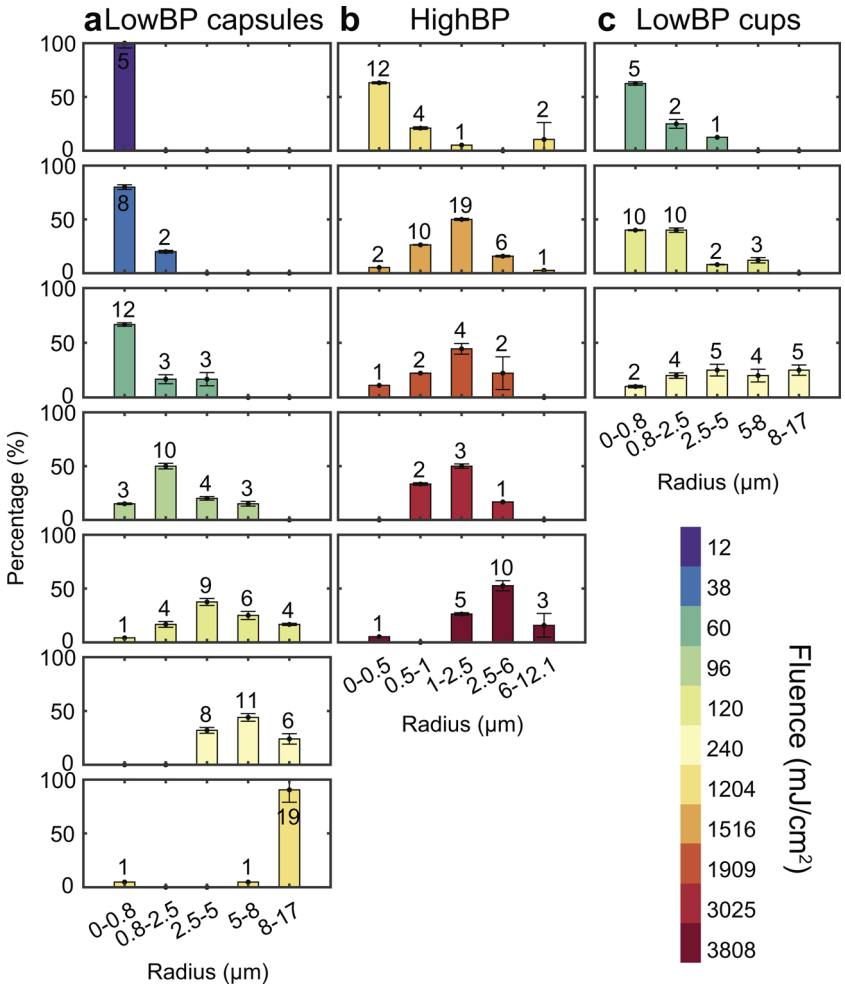

Fig. 9. Maximum bubble radius. Maximum radius of the bubble produced by (**a**) low BP (Resomer-PFP) capsules, (**b**) highBP (PMMA-Hexadecane) capsules and (**c**) lowBP (Resomer-PFP) cups for varying fluences. All particles here contain 5% w/w dye.

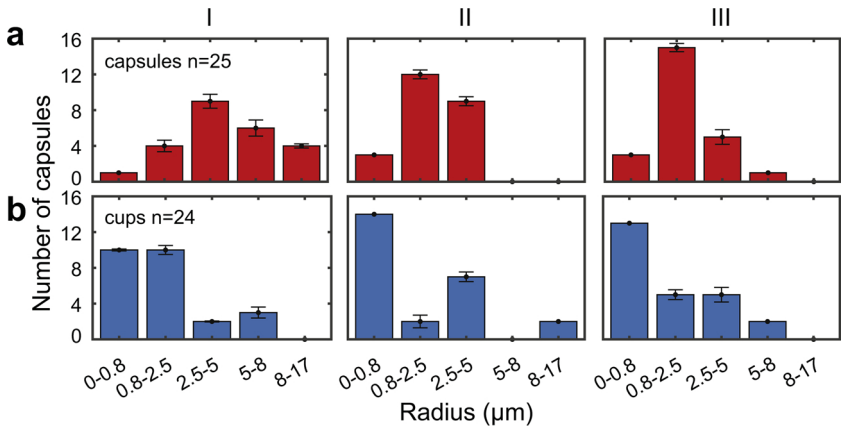

Fig. 10. Evolution of the lowBP (Resomer-PFP) particle response over three laser pulses. Maximum bubble radius lowBP (**a**) capsules and (**b**) cups at a laser fluence of 120 mJ/cm^2, showing the evolution of the response over three laser pulses.

5. Discussion

5.1. Particle size

The particles used in this study are 3 μm in radius. Ultimately, the desired size is sub-micrometric. The model can predict the bubble size generated by smaller particles in relation to the frequency of the acoustic response. The result is displayed in Fig. 13 for both types of particles. The characteristic curve (center frequency versus bubble radius) is fairly independent of the initial particle size for the HighBP particles where only water is vaporized. The emitted frequencies, however, increase significantly as the particle size decreases. These higher frequencies still fall within the medical range and would even allow for a better resolution for the monitoring of cavitation. The general trend also holds for the LowBP particles, although it is clear that the presence of the low boiling point core lowers the emitted

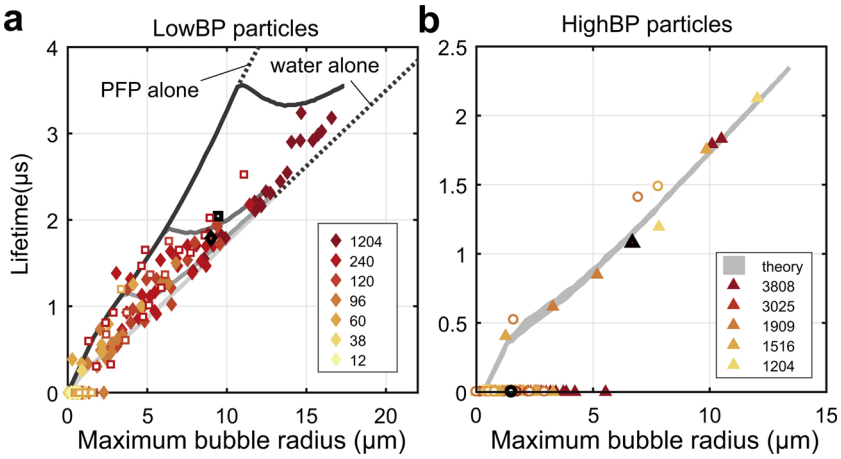

Fig. 11. Bubble lifetime versus maximum bubble radius. Bubble lifetime as a function of the maximum bubble radius for (**a**) lowBP (Resomer-PFP) (♦) capsules and (□) cups and for (**b**) highBP (PMMA-hexadecane) capsules containing (▲) 5% dye and (○) 3% dye. The solid lines are the theoretical predictions with a partial oil content of 10%, 40%, 60% and 100% (from light grey to black) of the expected amount as calculated from the capsules formulations. The legend gives the experimental laser fluences in mJ/cm^2. The thick black symbols represent the experiments depicted in Fig. 6 and 8 (in **a**) and Fig. 7 (in **b**.).

frequencies as compared to similar bubble sizes as in Fig. 13b. This effect is most pronounced for small particles. Note that, for a given particle size, the influence of the core vanishes as the cavitation bubbles get larger, namely, as their dynamics become dominated by water vapor.

5.2. Numerical model

In the numerical simulations, the surface tension was set to zero when the cavitation bubble is smaller than the capsule, to represent a shielding from the polymer shell as the bubble grows. This shielding makes the simulation results consistent when changing the size of the initial nucleus (nucleation is not part of the proposed thermodynamic model) and matches the observations. This shielding does not influence the response to higher energy activations in the simulations.

A choice was made here to treat the two configurations of lowBP particles as a single entity in the simulation. This simplification, however, has very little impact on the outcome of the numerical integration. The only numerical difference is the choice of the polymer thickness, i.e. the timescale for heat transfer from the polymer to the vapor, which remains short ($\sim$0.25 μs) as compared to the observed dynamics.

In the numerical model, where we vary the R_{int}/R_{ext} ratio, the first and third slopes (see Fig. 5) are similar for all curves, indicating bubble growth due to vaporization of the oil (first slope) and the water (third slope). The plateau is thus a transition regime where all the oil is vaporized and where the capsule does not have enough energy to vaporize the water. The length of this plateau decreases for increasing R_{int}/R_{ext} ratio, as a result of the increasing volume of oil available in the core. Also as a result of this, the maximum size of the vapor bubbles first increases as a function of R_{int}/R_{ext}, before decreasing as the amount of energy that can be stored in the polymer becomes insufficient to support the growing bubble.

Lower R_{int}/R_{ext} ratios render the high boiling point capsules more effective, though this effect is minimal. These thick capsules, however, will be practically more difficult to break and therefore to activate. This nucleation issue for thick capsules is not taken into account in this model.

5.3. Experimental vaporization dynamics

The vaporization threshold, which can be seen in Fig. 9, is significantly lower for lowBP capsules than for highBP capsules: 38 mJ/cm^2 versus 1204 mJ/cm^2 . The threshold for highBP capsules is expected to be higher, since it relies on the vaporization of water. Additionally, the polymer needs to melt in order to create a nucleation site for the bubble [21], and the resomer melts around 50 °C while PMMA melts at a temperature of 102 °C. Furthermore, from the optical measurements, the lowBP capsules appeared darker than the highBP capsules, suggesting that the uptake of dye is more efficient in the resomer than in the PMMA. All these factors contribute to the dramatic difference in activation threshold between the two types of capsules.

In this study, we prepared two formulations for the HighBP capsules: one loaded with 3% dye and one loaded with 5% dye. Both were investigated experimentally. However, the dye content makes no difference for the vaporization process, as confirmed by the model, except for lowering the activation threshold. Indeed, both types of capsules follow the expected behavior in Fig. 11 and 12, regardless of the dye concentration.

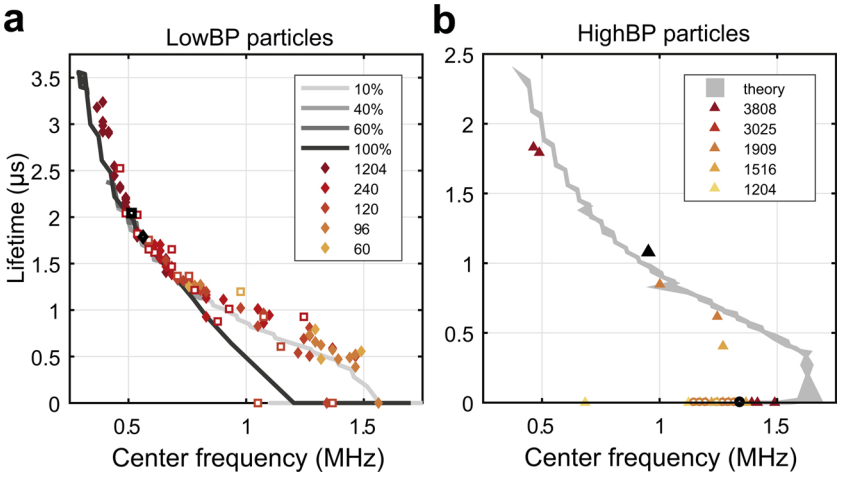

Fig. 12. Bubble lifetime as a function of center frequency. Lifetime as a function of center frequency for (**a**) for Resomer-PFP (lowBP) (♦) capsules and (□) cups and (**b**) PMMA-hexadecane (HighBP) capsules containing (▲) 5% dye and (○) 3% dye. The theoretical predictions for the latter include a partial vaporization of the oil. The legend gives the experimental laser fluences in mJ/cm^2. The thick black symbols represent the experiments depicted in Fig. 6 and 8 (in **a**) and Fig. 7 (in **b**.).

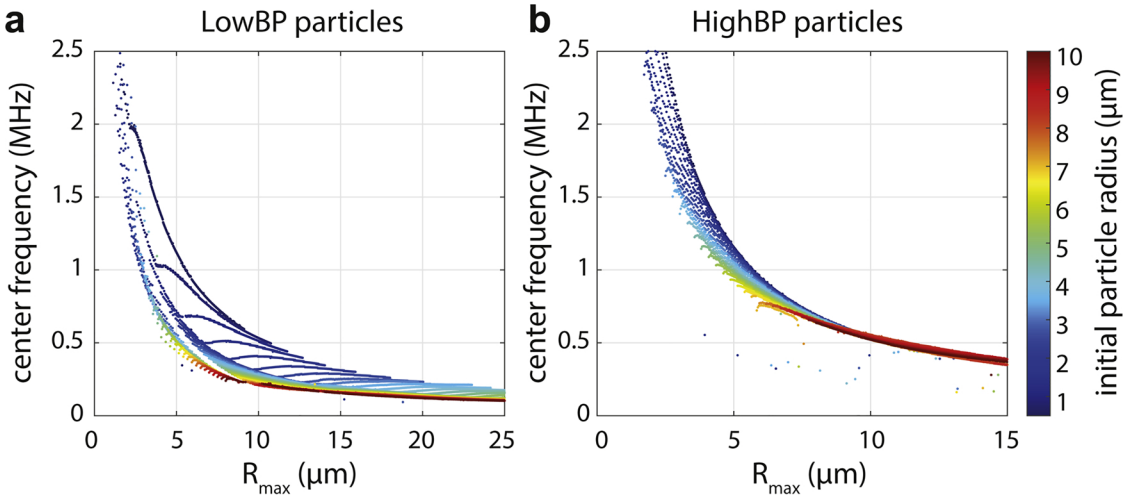

Fig. 13. Center frequency versus bubble size as a function of the initial particle radius predicted by the proposed model for (**a**) the LowBP particles and (**b**) the HighBP particles.

Internal bubbles produced by highBP capsules is a phenomenon that we believe results from the large temperature reached inside the shell due to the spherical divergence of the heat flux, which is potentially enhanced by the presence of dye crystals in the polymer. As a result, the temperature can be locally increased and reach the depolymerization temperature of the shell, which leads to gas formation [29]. The shell remains otherwise intact which prevents further vaporization.

The comparison between the numerical model and the experiments strongly suggests a loss of perfluoropentane during production of the capsules; high volatility of PFP and small dimensions of the droplets could allow for a partial diffusion/evaporation of the PFP. This hypothesis is consistent with the relatively smaller size of the PFP-filled particles as compared to the Hexadecane-filled particles. This is further confirmed by the very good agreement on the vaporization dynamics observed in Figs. 6 and 8 when accounting for a partial content of PFP. Additionally, there is a possibility that the violent dynamics involved in the early growth of the bubble separates the vapor nucleus from all, or part, of the oil core, thereby canceling its enhancing effect.

As a control, and to rule out the possible influence of entrapped gas bubble on the surface of the particles, we also irradiated a lowBP capsule sample that was degassed for over an hour. These capsules responded no differently than the native sample. We note as well that the entrapment of gas on such a smooth surface (as revealed by SEM) is unlikely.

5.4. Medical relevance

The particles used in this study have not been optimized for use in a clinical setting. However, there are possibilities to optimize these particles to lower the activation threshold. The absorption wavelength of the dye can for example be changed to the NIR window, allowing the use of relatively high laser fluences. From a chemistry/formulation standpoint, it is clear that the encapsulation efficiency of the dye may also be increased. We would like to point out that, despite the present lack of optimization, the low boiling point capsules are in fact activated significantly below the 100 mJ/cm^2 threshold permitted in the NIR. Regarding their sizes, the microcapsules are comparable to ultrasound contrast microbubbles, and therefore relevant as blood pool agents. However, micron-sized capsules do not have the capacity to extravasate. The production of sub-micrometer capsules, or nanocapsules, and the observation of their response are challenges in themselves. There, the numerical model, verified for micron-sized capsules provides valuable insights: particles with a size below 1 μm are expected to still produce bubbles with a maximum radius of several micrometers, which (see for example Fig. 13) are readily detected within the medically relevant frequency range.

5.5. Phase transition shift for small particles

Phase transition temperatures can shift with size. The melting temperature of gold nanorods, in particular, is known to be much lower than that of bulk gold. This shift, however, is only significant when the surface energy becomes comparable to the internal bulk energy. Following the Gibbs-Thomson derivation, the typical shift in vaporization temperature for a liquid drop (e.g. the capsule's core) would be $\Delta T = 4\sigma/\rho H d$ with σ the surface tension, d the capsule diameter, ρ the liquid density and H the phase change enthalpy. In this example the shift for a 1 μm capsule would reach 0.01% for water and 0.03% for perfluoropentane. The shift in vaporization temperature is therefore negligible.

6. Conclusions

In this paper, we have studied experimentally and theoretically two formulations and two configurations of light-responsive microparticles. The theory agrees well with the experimental data, although the lowBP capsules seem to vaporize less perfluoropentane than expected. This is nonetheless nicely captured in the model by lowering the amount of PFP available for vaporization. The capsules containing a high boiling point oil require a high threshold for activation ($\sim$1 J/cm^2) whereas the capsules loaded with a low boiling point oil have an activation threshold $\sim$30 times lower. The cups displayed a behavior that is very similar, in general, to that of the capsules but are much easier to fabricate. Finally, we observed that the dynamics of the microbubbles generated by both types of capsules is influenced by their content but remain within the same range: in a nut shell, $\sim$10 μm bubbles, living $\sim$2.5 μs and, emitting acoustic bursts with a center frequency of 0.5 to 1.5 MHz. These frequencies are highly relevant for medical applications and the pressure level obtained from a single event can readily be detected by standard ultrasound transducers.

Conflicts of interest

The authors declare no conflicts of interest.

Acknowledgements

This work is supported by NanoNextNL, a micro and nanotechnology consortium of the Government of the Netherlands and 130 partners. We gratefully acknowledge the continuous support of Gert-Wim Bruggert, Bas Benschop and Martin Bos on the technical aspects.

Appendix A. Supplementary data

Supplementary data associated with this article can be found, in the online version, at https://doi.org/10.1016/j.pacs.2020.100185.

References

[1] C.D. Ohl, M. Arora, R. Dijkink, V. Janve, D. Lohse, Surface cleaning from laser-induced cavitation bubbles, Appl. Phys. Lett. 89 (2006) 74102.
[2] J. Collis, R. Manasseh, P. Liovic, P. Tho, A. Ooi, K. Petkovic-Duran, Y. Zhu, Cavitation microstreaming and stress fields created by microbubbles, Ultrasonics 50 (2010) 273–279.
[3] C.E. Brennen, Cavitation and Bubble Dynamics, Oxford University Press, New York, 1995.
[4] F. Caupin, E. Herbert, Cavitation in water: a review, Comptes Rendus Physique 7 (2006) 1000–1017.
[5] Z.G. Li, S. Xiong, L.K. Chin, K. Ando, J.B. Zhang, A.Q. Liu, Water's tensile strength measured using an optofluidic chip, Lab. Chip 15 (2015) 2158–2161.
[6] J.J. Rassweiler, T. Knoll, K.-U. Köhrmann, J.A. McAteer, J.E. Lingeman, R.O. Cleveland, M.R. Bailey, C. Chaussy, Shock wave technology and application: an update, Eur. Urol. 59 (2011) 784–796.
[7] J. Qin, W.N. Simmons, G. Sankin, P. Zhong, Effect of lithotripter focal width on stone comminution in shock wave lithotripsy, J. Acoust. Soc. Am. 127 (2010) 2635–2645.
[8] B. Petit, E. Gaud, D. Colevret, M. Arditi, F. Yan, F. Tranquart, E. Allemann, In vitro sonothrombolysis of human blood clots with BR38 microbubbles, Ultrasound Med. Biol. 38 (2012) 1222–1233.
[9] M.T. Burgess, T.M. Porter, Acoustic cavitation-mediated delivery of small interfering ribonucleic acids with phase-shift nano-emulsions, Ultrasound Med. Biol. 41 (2015) 2191–2201.
[10] M. Bazan-Peregrino, C.D. Arvanitis, B. Rifai, L.W. Seymour, C.-C. Coussios, Ultrasound-induced cavitation enhances the delivery and therapeutic efficacy of an oncolytic virus in an in vitro model, J. Control. Release 157 (2012) 235–242.
[11] M. Bazan-Peregrino, B. Rifai, R.C. Carlisle, J. Choi, C.D. Arvanitis, L.W. Seymour, C.C. Coussios, Cavitation-enhanced delivery of a replicating oncolytic adenovirus to tumors using focused ultrasound, J. Control. Release 169 (2013) 40–47.
[12] Reznik, R. Williams, P.N. Burns, Investigation of vaporized submicron perfluorocarbon droplets as an ultrasound contrast agent, Ultrasound Med. Biol. 37 (2011) 1271–1279.
[13] N. Reznik, M. Seo, R. Williams, E. Bolewska-Pedyczak, M. Lee, N. Matsuura, J. Gariepy, F.S. Foster, P.N. Burns, Optical studies of vaporization and stability of fluorescently labelled perfluorocarbon droplets, Phys. Med. Biol. 57 (2012) 7205–7217.
[14] N. Reznik, O. Shpak, E.C. Gelderblom, R. Williams, N. de Jong, M. Versluis, P.N. Burns, The efficiency and stability of bubble formation by acoustic vaporization of submicron perfluorocarbon droplets, Ultrasonics 53 (2013) 1368–1376.
[15] K. Wilson, K. Homan, S. Emelianov, Biomedical photoacoustics beyond thermal expansion using triggered nanodroplet vaporization for contrast-enhanced imaging, Nat. Commun. 3 (2012) 618.
[16] R. Xiong, S.K. Samal, J. Demeester, A.G. Skirtach, S.C. De Smedt, K. Braeckmans, Laser-assisted photoporation: fundamentals, technological advances and applications, Adv. Phys.: X 1 (2016) 596–620.
[17] J.J. Kwan, R. Myers, C.M. Coviello, S.M. Graham, A.R. Shah, E. Stride, R.C. Carlisle, C.C. Coussios, Ultrasound-propelled nanocups for drug delivery, Small 11 (2015) 5305–5314.
[18] Y. Wang, M.E. Zaytsev, G. Lajoinie, H.L. The, J.C.T. Eijkel, A. van den Berg, M. Versluis, B.M. Weckhuysen, X. Zhang, H.J.W. Zandvliet, D. Lohse, Giant and explosive plasmonic bubbles by delayed nucleation, Proc. Natl. Acad. Sci. USA 115 (2018) 7676–7681.
[19] G. Lajoinie, T. van Rooij, I. Skachkov, E. Blazejewski, G. Veldhuis, N. de Jong, K. Kooiman, M. Versluis, Laser-activated polymeric microcapsules for ultrasound imaging and therapy: in vitro feasibility, Biophys. J. 112 (2017) 1894–1907.
[20] M. Visscher, G. Lajoinie, E. Blazejewski, G. Veldhuis, M. Versluis, Laser-activated microparticles for multimodal imaging: ultrasound and photoacoustics, Phys. Med. Biol. 64 (2019) 34001.
[21] G. Lajoinie, E. Gelderblom, C. Chlon, M. Böhmer, W. Steenbergen, N. de Jong, S. Manohar, M. Versluis, Ultrafast vapourization dynamics of laser-activated polymeric microcapsules, Nat. Commun. 5 (2014) 3671.
[22] C. Antoine, Tensions des vapeurs; nouvelle relation entre les tensions et les températures, Comptes Rendus Des Séances de l'Académie Des Sciences 107 (1888) 681–684.
[23] C.-T. Liu, W.T. Lindsay, Vapor pressure of deuterated water from 106 to 300 deg, J. Chem. Eng. Data 15 (1970) 510–513.
[24] J.B. Keller, M. Miksis, Bubble oscillations of large amplitude, J. Acoust. Soc. Am. 68 (1980) 628–633.
[25] A. Prosperetti, A. Lezzi, Bubble dynamics in a compressible liquid. Part 1. First-order theory, J.Fluid Mech. 168 (1986) 457–478.
[26] A. Loxley, B. Vincent, Preparation of poly(methylmethacrylate) microcapsules with liquid cores, J. Colloid Interface Sci. 208 (1998) 49–62.
[27] C.T. Chin, C. Lancée, J. Borsboom, F. Mastik, M.E. Frijlink, N. de Jong, M. Versluis, D. Lohse, Brandaris 128: A digital 25 million frames per second camera with 128 highly sensitive frames, Rev. Sci. Instrum. 74 (2003) 5026–5034.
[28] E.C. Gelderblom, H.J. Vos, F. Mastik, T. Faez, Y. Luan, T.J.A. Kokhuis, A.F.W. van der Steen, D. Lohse, N. de Jong, M. Versluis, Brandaris 128 ultra-high-speed imaging facility: 10 years of operation, updates, and enhanced features, Rev. Sci. Instrum. 83 (2012) 103706.
[29] K. Smolders, J. Baeyens, Thermal degradation of PMMA in fluidised beds, Waste Manag. 24 (2004) 849–857.

Guillaume Lajoinie received his M.Sc degrees from Ecole Centrale of Lyon (physics) and University Claude Bernard in Lyon (medical imaging and instrumentation) in 2011, with a focus on micro and nanotechnology. During his PhD (University of Twente, 2015), he specialized in the design and physical study of innovative contrast agents for ultrasound and photoacoustics and their applications. To that end, he investigated microscale flows, phase-change, acoustic contrast and cavitation using various experimental techniques, and in particular ultra-high-speed imaging. He is now assistant professor in the Physics of Fluids group of the University of Twente and works on microscale physics, microbubbles, heat and mass transfer and quantitative plane-wave ultrasound.

Mirjam Visscher earned her Bachelor degree in the Biomedical Photonic Imaging group at the University of Twente, The Netherlands, on the subject of photothermal mechanisms in tumor-simulating beads embedded with gold nanorods. During her studies, she developed interest in medical physics. She finished her Master degrees in Biomedical Engineering in the Physics of Fluids group, University of Twente, where she investigated polymeric microcapsules for multimodal imaging. Her current Ph.D. position is in the Biomedical Engineering group, Erasmus Medical Center in Rotterdam where she focuses on the assessment of atherosclerosis plaques using photoacoustic spectroscopy and MALDI imaging mass spectrometry.

Emilie Blazejewski joined Nanomi B.V, a subsidiary of Lupin Pharmaceuticals, in October 2013. She started as development engineer within the formulation group and spent 6 years developing complex injectables drug products, mostly focusing on encapsulation of small drug molecule within polymeric matrix. Since October 2019, she is part of the Nanomi management team as Head of formulation and process department.

Gert Veldhuis, PhD, graduated in Applied Physics from the University of Twente and obtained his PhD cum laude at the MESA + Research Institute of the University of Twente. He worked at Philips Research and Alcatel before he founded Nanomi in 2004. Nanomi is a pharmaceutical nanotech company specialized in the formulation, development and manufacturing of sustained release complex injectable products. He acted as managing director until the company was acquired by Lupin. Today, Dr. Veldhuis serves as CBDO at U-Needle, an emerging medical device company in the field of intradermal drug delivery.

Michel Versluis received his M.Sc. degree in physics from the University of Nijmegen, The Netherlands in 1988 with a special interest in molecular physics and astrophysics. Later, he specialized in the application of ultraviolet lasers for flame diagnostics (PhD, Nijmegen 1992), for molecular dynamics (Griffth University, Brisbane, Australia), for internal combustion engines (Lund, Sweden), industrial jet flames and solid rocket propellants (Delft, The Netherlands). He is currently a Full Professor of Physical and Medical Acoustics in the Physics of Fluids Group, University of Twente, The Netherlands. He is an expert in ultra-high-speed imaging with a particular interest in the use of microbubbles and microdroplets for medical applications, both in imaging and in therapy.